Computational Materials Science 141 (2018) 49–58

Contents lists available at ScienceDirect

Computational Materials Science

journal homepage: www.elsevier.com/locate/commatsci

Elastic properties and thermal expansion of lead-free halide double perovskite $Cs_2AgBiBr_6$

Liyuan Dong [a], Shijing Sun [b], Zeyu Deng [b], Wei Li [a,*], Fengxia Wei [b,*], Yajun Qi [c,*], Yanchun Li [d], Xiaodong Li [d], Peixiang Lu [a,e], U. Ramamurty [f,*]

[a] School of Physics and Wuhan National Laboratory for Optoelectronics, Huazhong University of Science and Technology, Wuhan 430074, China
[b] Department of Materials Science and Metallurgy, University of Cambridge, Cambridge CB3 0FS, UK
[c] Department of Materials Science and Engineering, Hubei University, Wuhan 430062, China
[d] Institute of High Energy Physics, Chinese Academy of Sciences, Beijing 100049, China
[e] Laboratory for Optical Information Technology, Wuhan Institute of Technology, Wuhan 430205, China
[f] Department of Materials Engineering, Indian Institute of Science, Bangalore 560012, India

ARTICLE INFO

Article history:
Received 2 June 2017
Received in revised form 12 June 2017
Accepted 5 September 2017

Keywords:
Lead-free halide double perovskite
Elastic properties
Thermal expansion
Density functional theory

ABSTRACT

The elastic properties and thermal expansion behavior of lead-free halide double perovskite, $Cs_2AgBiBr_6$, were studied first with the aid of first principles calculations, which were followed by experimental characterization. The calculated full elastic constants enable the complete mapping of Young's and shear moduli, and Poisson's ratios of $Cs_2AgBiBr_6$ along all crystallographic orientations. Results show that significant anisotropy in them despite the fact that $Cs_2AgBiBr_6$ possesses cubic symmetry. Detailed structural analysis and a spring model were utilized to rationalize the observed anisotropy. Further, the theoretical results were validated by recourse to nanoindentation and high-pressure synchrotron powder X-ray diffraction experiments. The superior mechanical behavior of $Cs_2AgBiBr_6$ over the hybrid bromide analogues, $MAPbBr_3$ ($MA = CH_3NH_3^+$), were attributed to the higher framework stiffness of the former, which is a result of the presence of relatively stronger Ag-Br and Bi-Br bonds in it. Variable temperature single crystal X-ray diffraction reveal linear and volumetric thermal expansion coefficients to be about 20% lower than those of $MAPbBr_3$, again suggesting its higher framework rigidity. The superior stiffness, thermal expansion behavior, moisture stability, and nontoxicity of $Cs_2AgBiBr_6$ make it a strong candidate for potential applications in optoelectronics and photovoltaics.

1. Introduction

It has been shown in the recent past that substantially high solar energy conversion efficiencies can be achieved by utilizing hybrid organic–inorganic perovskites (HOIPs). As a result, these materials are attracting considerable research interest, especially from the photovoltaic research community. Additionally, processing of these materials is relatively simple, making their cost lower [1–4]. However, the most efficient HOIPs reported thus far are lead-based compounds with $APbI_3$ stoichiometry in which the A-site cations are either $CH_3NH_3^+$ (MA) [5–7] or $(H_2N)_2CH^+$ (FA) [8]. Naturally, the presence of Pb is a serious concern from the environment point of view [1,9]. Moreover, they face stability issues upon long term exposure to sunlight, humidity in atmospheric conditions, and elevated temperatures during functioning [1]. An additional impediment to the widespread deployment of HOIPs in solar energy technology is their low mechanical resistance, which could have adverse effect on their in-service reliability. To overcome these shortcomings, nontoxic perovskite halides, wherein the divalent Pb is replaced with the combination of monovalent and trivalent metals to form double perovskites, are being explored. In this pursuit, several double perovskite systems that include hybrid $[MA]_2[KBiCl_6]$ [10], $[MA]_2[TlBiBr_6]$ [11], and $[MA]_2[AgBiBr_6]$ [11,12], and inorganic $Cs_2AgBiCl_6$, $Cs_2AgBiBr_6$ [13–17], and $Cs_2AgInCl_6$ [18] have been identified as potential alternatives. Amongst these, $Cs_2AgBiBr_6$ not only has high light absorbing efficiency in the visible range of the solar spectrum but also exhibits impressive moisture stability in air. Hence, it is a possible candidate that could be used in tandem systems with Si cells. However, its thermal expansion and mechanical properties, which are crucial for successful technological development, have not been examined. In particular the anisotropy in these properties needs to be ascertained, as high anisotropy can be

* Corresponding authors.
E-mail addresses: wl276@hust.edu.cn, wl276@outlook.com (W. Li).

http://dx.doi.org/10.1016/j.commatsci.2017.09.014
0927-0256/

detrimental for residual stress management and hence long term reliability in service. Keeping this in view, we have performed a comprehensive theoretical study on the elastic behavior of $Cs_2AgBiBr_6$ with the aid of the density functional theory (DFT) calculations, whose predictions were experimentally verified by techniques such as nanoindentation, high-pressure synchrotron powder X-ray diffraction (HP-PXRD). Moreover, this materials's thermal expansion properties were revealed *via* variable temperature single crystal X-ray diffraction (VT-SCXRD) experiments. In this process, we uncover the high framework stiffness, significant elastic anisotropy, low thermal expansion of $Cs_2AgBiBr_6$ and the underlying structural origins.

2. Theoretical and experimental details

2.1. DFT calculations

The DFT calculations were first carried out so as to optimize the lattice parameters and calculate the elastic constants (C_{ij}) of $Cs_2AgBiBr_6$ using Cambridge Sequential Total Energy Package (CASTEP). The electron wave function was expanded through the plane wave basis set, and the ultrasoft pseudopotentials were adopted to build the effective interaction between the valence electrons and the atomic cores, which bring greater flexibility and smoother pseudo-wavefunctions, which in turn enable the usage of considerably fewer plane-waves for calculations without compromising on accuracy [19]. The PBEsol parameterization in the generalized gradient approximation (GGA) (Table 1) [20] and other parameterizations (Table S1) were taken as the exchange - correlation potentials of e-e interactions [21–23]. Previous DFT works on Pb-free halide double perovskites have shown that the influence of spin–orbit coupling and spin polarization on structural and mechanical properties is insignificant [24,25]. Therefore, these were not taken into consideration in the current computational study. For geometry optimization and energy calculations performed in the reciprocal space, the energy cut off was set to 350 eV. The Brillouin Zone integration was approximated using a $4\times4\times4$ *k*-point mesh sampling scheme of Monkhorst – Pack [26] whereas the fast Fourier transform grid was set as $48\times48\times48$. The Broyden - Fletcher - Goldfarb - Shanno (BFGS) minimization scheme was used to optimize the crystal structure at 0 GPa for the elastic constants calculations [27], and the optimization was implemented through the relaxation of both the lattice parameters and atomic positions. All atoms were fully relaxed until residual forces on constituent atoms become smaller than 0.05 eV/Å in geometry optimization and 0.01 eV/Å in calculating C_{ij}, with the convergence criteria for maximum atomic displacement being set at 2×10^{-3} Å for geometry optimization and 4×10^{-4} Å in calculating C_{ij}, and the internal stress was less than 0.1 GPa. The elastic constants of single crystals were calculated by employing the finite - strain method [28] and by setting the maximum strain amplitude and the number of steps as 0.003 and 9 for each strain, respectively.

2.2. Synthesis of the single crystals

All chemicals and solvents used in this study were of reagent grade or higher purity, purchased from commercial vendors and are used in the as-received condition. Single crystals of $Cs_2AgBiBr_6$ were synthesized using the method already described in the literature, which is briefly described in the following [13,29]. First, CsBr (0.426 g, 2 mmol), $BiBr_3$ (0.449 g, 1 mmol) and AgBr (0.188 g, 1 mmol) were added into a 23 mL Teflon-lined autoclave, then 12.8 mL of 7 mol/L HBr acid was added and the mixture was stirred for 10 min. The autoclave was then heated to 190 °C and held at that temperature for 10 h, before cooling at the rate of 4 °C/h from 190 to 110 °C, and then at 0.5 °C/h from 110 to 80 °C, before cooling to room temperature. Orange red crystals were harvested from the solution after cooling with a yield of about 55% based on Bi [13,29].

2.3. Face indexing and nanoindentation

Single crystals of $Cs_2AgBiBr_6$ with well-defined octahedral shape were selected and the natural face (1 1 1) was indexed by single crystal X-ray diffraction (SCXRD) using an Oxford Diffraction Rigaku XtaLAB mini™ diffractometer with Mo-Kα radiation (λ = 0.71073 Å) at 300 K (Fig. S1). The nanoindentation experiments were performed by employing a sharp Berkovich tip [30,31], and the indenter axis was aligned normal to the (1 1 1) plane. The loading/unloading rates and the holding time at peak load were maintained at 0.5 mN/s and 10 s, respectively. A fused silica standard with a reduced modulus of 72 GPa and hardness of 9 GPa was used for calibration. Young's modulus (E_s) and indentation hardness (H) of the $Cs_2AgBiBr_6$ crystals were obtained from the *P-h* plots (Fig. S2) using the standard Oliver-Pharr Method (Table S3) [32].

Table 1
Halogen atom populations, lattice parameters, elastic constants and derived elastic properties of Cs_2AgBiX_6 (X = Cl, Br or I) obtained from the first principles calculations.

Properties	Quantities	Cl	Br	I
Halogen atom populations, (e)	Mulliken	−0.49	−0.18	−0.06
	Hirshfeld	−0.18	−0.15	−0.12
Lattice parameter, *a* (Å)		10.67	11.19	12.03
Stiffness coefficient, C_{ij} (GPa)	C_{11}	66.70	59.02	43.68
	C_{12}	15.61	13.37	9.04
	C_{44}	8.85	8.15	7.48
Young's modulus, *E* (GPa)	$E_{max} = E(1\,0\,0)$	60.78	54.08	40.58
	$E(1\,1\,0)$	28.63	26.17	22.91
	$E_{min} = E(1\,1\,1)$	24.34	22.33	20.01
Shear modulus, *G* (GPa)	$G(1\,0\,0)\langle h\,k\,l\rangle$	8.85	8.15	7.48
	$G(1\,1\,1)\langle h\,k\,l\rangle$	15.68	14.26	12.04
	$G_{max} = G(1\,1\,0)\langle 1\,-1\,0\rangle$	25.55	22.82	17.32
	$G_{min} = G(1\,1\,0)\langle 0\,0\,1\rangle$	8.85	8.15	7.48
Poisson's ratio, *v*	$v < 100,h\,k\,l>$	0.19	0.18	0.17
	$v < 111,h\,k\,l>$	0.38	0.37	0.34
	$v_{max} = v<110,1-10>$	0.62	0.61	0.53
	$v_{min} = v<110,001>$	0.09	0.09	0.09
Anisotropy index	Zener, *A* (=1 if isotropic)	2.89	2.80	2.32
Bulk modulus, *B* (GPa)		32.64(58)	28.58(12)	20.58(35)

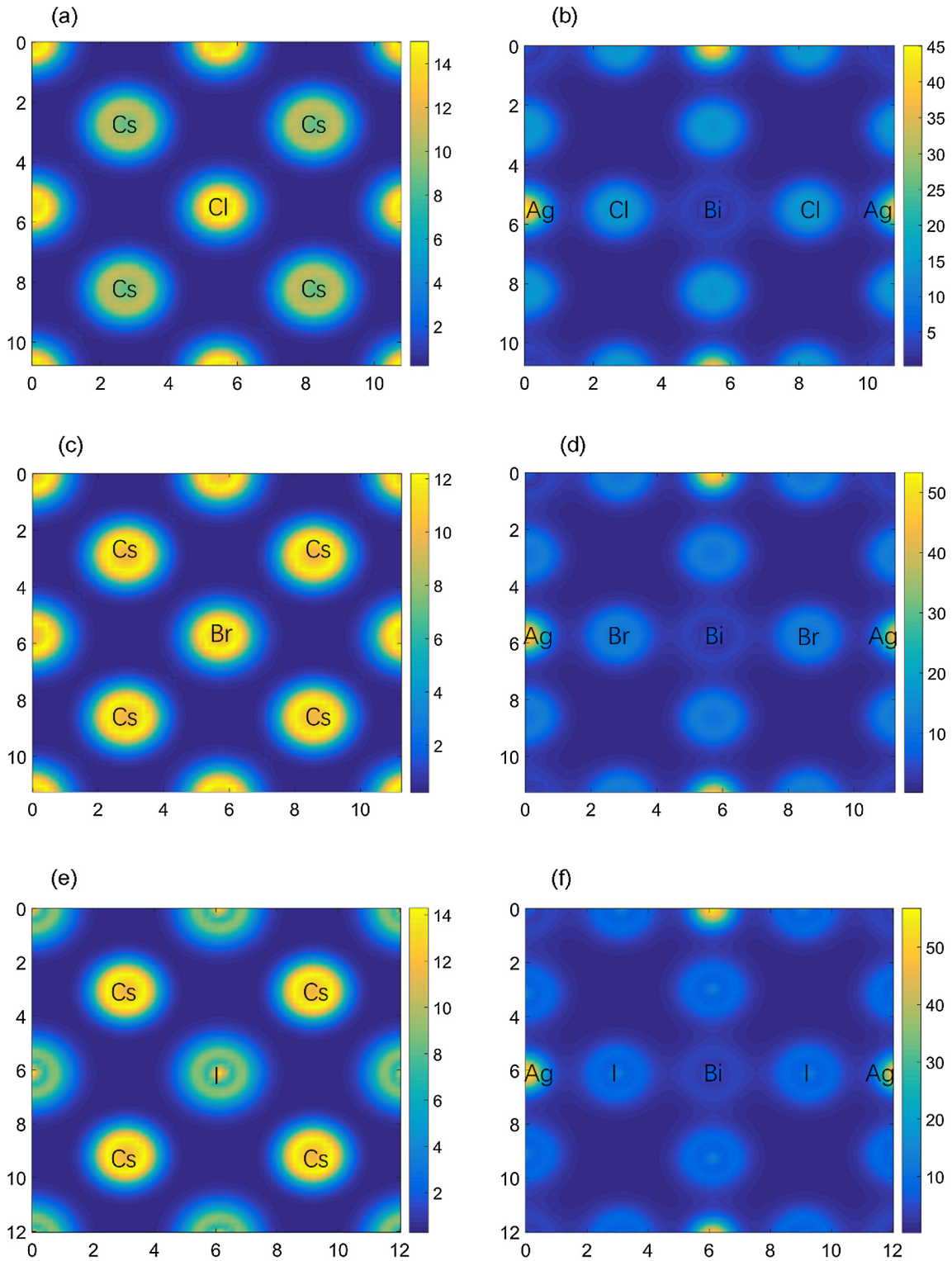

Fig. 1. 2D horizontal cross section color-contour graphics of charge density distributions of Cs_2AgBiX_6. The pictures are projected onto the (0 0 1) plane, (a), (c), (e) and (b), (d), (f) represent orientations passing through the Cs-X and Ag-Bi-X planes, respectively [38]. Note the charge density ($Å^{-3}$) marked by color bar only has relative meanings in each picture.

2.4. Synchrotron experiments

The structural aspects of $Cs_2AgBiBr_6$ with pressure were studied *via* HP-PXRD over the range of 0–1.57 GPa at the 4W2 beam line in the Beijing Synchrotron Radiation Facility (BSRF). An X-ray beam with a wavelength of 0.61992 Å that was focused on an area of 36×12 μm^2 by using Kirkpatrick-Baez mirrors from 0 to 25° incident angle was utilized. The hydrostatic pressure was imposed by a diamond anvil cell (DAC) with a 400 μm culet diameter. Well ground powder samples were placed in ~120 μm diameter hole in

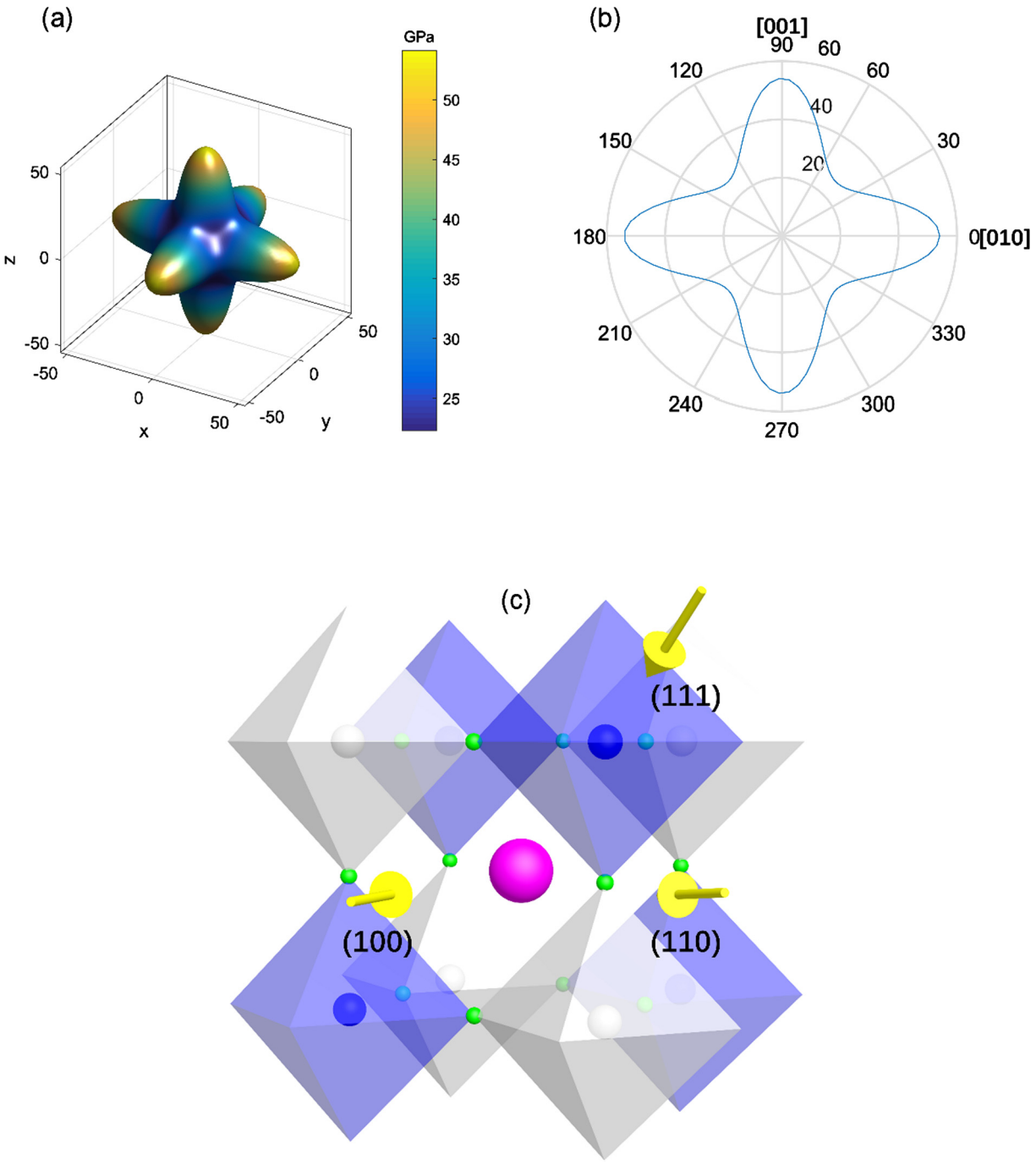

Fig. 2. Young's modulus (E) representation surfaces extracted from DFT calculations. (a) 3D surface. (b) 2D polar plots of E projected normal to the (1 0 0) plane. 0 and 90° are along the [0 1 0] and [0 0 1], respectively. (c) Perovskite structure of $Cs_2AgBiBr_6$. Color codes: Bi, blue; Ag, gray; Cs, rose; Br, green. The arrows indicate the uniaxial stresses loaded normal to the (1 0 0) (left arrow), (1 1 0) (right arrow), and (1 1 1) (top right arrow) planes, respectively. (For interpretation of the references to color in this figure legend, the reader is referred to the web version of this article.)

a pre-indented stainless steel gasket with a ~40 μm thickness. Silicone oil was used as the pressure transmission medium. Ruby chips were utilized for pressure calibration by measuring its fluorescence shift that is a known function of pressure. The diffraction patterns were recorded by a Pilatus3 2M detector that was integrated with the FIT2D software package. The cell parameters of powder patterns collected at each pressure point were refined by Le-Bail whole profile fitting method using the Total Pattern Solution (TOPAS) software.

2.5. Variable temperature single crystal X-ray diffraction

The thermal expansion behavior of $Cs_2AgBiBr_6$ was studied via VT - SCXRD experiments using an Oxford Diffraction Gemini E Ultra diffractometer with Mo - Kα radiation (λ=0.71073 Å). The reduction and refinement of the data collected so as to determine the structural parameters as a function of temperature were performed by using the CrysAlis^{Pro} software. All the structures were solved using direct methods and successive Fourier difference

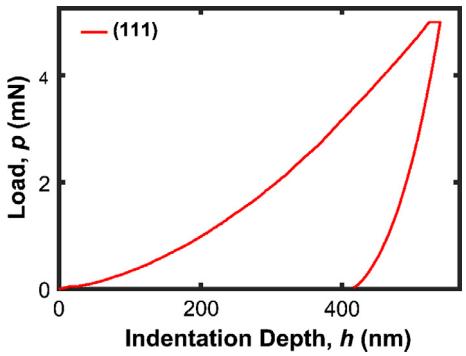

Fig. 3. Representative load-indentation depth (*P*-*h*) curve normal to the (1 1 1) plane [43].

analysis, and refined by full matrix least-squares procedure on F^2 with anisotropic thermal parameters for all atoms, using the OLEX 2 software. Crystallographic data for VT - SCXRD have been deposited at the Cambridge Crystallographic Data Centre (1531089–1531097).

2.6. Transmission electron microscopy (TEM)

Single crystals of $Cs_2AgBiBr_6$ were crushed and ground into fine powders, then a small amount of the powder diluted in ethanol was sonicated and dispersed for about 15 min. Then the suspensions were dipped onto a perforated carbon foil supported on a copper grid. Selected area electron diffraction (SAED) patterns normal to the (1 1 1) and (1 1 −2) planes were obtained on a Tecani G20 electron microscope operated at 200 kV under ambient temperature, which confirm the single crystallinity of the measured samples with an indexed lattice parameter of 11.24 Å [13,14,29].

3. Results and discussion

3.1. Elastic properties

The atomic positions within the crystal lattice, the lattice parameters (a), elastic constants (C_{ij}), calculated using DFT for three different lead-free halide double perovskites Cs_2AgBiX_6 (X = Cl, Br or I), are all listed in Table 1. Results of the additional calculations, which were performed using other exchange–correlation potentials, are listed in Table S1 of the supporting information (SI) for comparison. The three independent elastic stiffness coefficients C_{11}, C_{12} and C_{44}, obtained from DFT, satisfy the fundamental elastic stability criteria for cubic crystals, i.e., $C_{11} > |C_{12}|$, $C_{11} + 2C_{12} > 0$, and $C_{44} > 0$ [33–36]. The values of Young's moduli (E), shear moduli (G), Poisson's ratios (ν), anisotropy indexes (A) and bulk moduli (B) estimated using C_{ij} are also listed in Table 1 [37].

From Table 1, it is observed that the Mulliken or Hirshfeld charge, C_{ij}, E, G, and B scale inversely with the ionic radii of the halides. This trend is attributed to the decreasing Mulliken or Hirshfeld charge and electronegativity from chlorine to bromine, and then iodine in Cs_2AgBiX_6. This is because a reduced electronegativity lowers the strengths of the Ag-X and the Bi-X bonds. To further support this hypothesis, 2D horizontal cross sectional images of the charge density distributions in a 2×2 conventional cell are displayed in Fig. 1 [39–41]. From Fig. 1 (a), (c), and (e), it is seen that all the electrons of Cs and X surround their respective nuclei, with no shared electrons between the A- and X-sites. This observation leads us to conclude that the interatomic interactions between Cs and X are exclusively electrostatic in nature, and this is why they are nearly-pure ionic. On this basis, it is reasonable to conclude that the number of the surrounding electrons become less as X goes from Cl to I, which is consistent with the calculated results of Mulliken or Hirshfeld charges and electronegativities. While this providing the rationale for the observed variations in the elastic properties of Cs_2AgBiX_6. Note, Fig. 1 (b), (d), and (f), however, indicate that sharing of electrons between Ag/Bi and X does indeed exists. This observation implies that the Ag-Br and Bi-Br bonds are relatively more covalent in nature. In addition, the charge density distributions of halogen atoms show an increasingly diffuse nature as X goes from Cl to I. This, in turn, weakens the corresponding Ag-X and Bi-X bonds and electrostatic interactions between Cs and halogen atoms [15]. Consequently, the calculated C_{ij} and other elastic properties are negative correlation with the size of the halogen atoms.

It is notable that the directions of the maximum (E_{max}) and minimum (E_{min}) of Young's moduli of Cs_2AgBiX_6 depend on the $(a_1^2a_2^2 + a_1^2a_3^2 + a_2^2a_3^2)$ as expounded by the tensorial analysis of a cubic system, where $\boldsymbol{a}$ (a_1, a_2, a_3) are direction cosines for any arbitrary direction $\boldsymbol{a}$. Accordingly, E is defined as $E^{-1} = a_i a_j a_k a_l S_{ijkl}$ in a general structure [37], and $E^{-1} = S_{11} - (2S_{11} - 2S_{12} - S_{44})(a_1^2a_2^2 + a_1^2a_3^2 + a_2^2a_3^2)$ in a cubic structure. When $2S_{11} - 2S_{12} - S_{44} > 0$, E_{max} and E_{min} occur along ⟨1 1 1⟩ and ⟨1 0 0⟩, respectively, while the converse is true for $2S_{11} - 2S_{12} - S_{44} < 0$. Variations of E in all directions of $Cs_2AgBiBr_6$ are represented graphically as 3D and sectional 2D diagrams in Fig. 2 (download elastic constants plotting programs in https://github.com/alfredldong/). From them, it is seen that the crystal is stiffest along ⟨1 0 0⟩ and most complaint along ⟨1 1 1⟩, with ⟨1 1 0⟩ exhibiting an intermediate stiffness between those extrema. A high ratio of $A_E = E_{max}/E_{min} = 2.42$

Table 2
Summary of experimental values of Young's moduli (E), hardnesses (H), bulk moduli (B), phase transition pressure (P_c) and linear thermal expansion coefficients (α) of eight inorganic and hybrid perovskites.

	Phase	Orientation	E (GPa)	H (GPa)	B (GPa)	P_c (GPa)	α (MK^{-1})	Reference
$Cs_2AgBiBr_6$	Cubic	(1 1 1)	22.6(6)	0.67(3)	27.3(14)	>1.57	27.8(3)	This work
$CsPbBr_3$	Orthorhombic	(1 0 1)	15.8(6)	0.34(2)	15.5[a]	–	37.7	[42,47]
$(MA)_2AgBiBr_6$	Cubic	(1 1 1)	7.9(14)	0.55(11)	7.7[a,b]	–	44	[12]
		(1 1 0)	8.4(17)	0.47(9)	8.2[a,b]	–	–	[12]
$(MA)_2KBiCl_6$	Trigonal	(0 0 1)	10.5(12)	0.39(7)	10.3[a,b]	–	–	[10]
$(MA)_2TlBiBr_6$	Cubic	(1 1 1)	12.8(19)	0.56(10)	12.5[a,b]	–	–	[11]
$MAPbI_3$	Tetragonal	(1 0 0)	10.4(8)	0.42(4)	10.2[a,b]	~0.3	43.3	[48–51]
		(1 1 2)	10.7(5)	0.46(6)	10.5[a,b]	–	–	[49]
$MAPbBr_3$	Cubic	(1 0 0)	17.7(6)	0.31(2)	14.0[a]	~0.4,~1.1	33.3	[49,52,53]
		(1 1 0)	15.6(6)	0.26(2)	12.4[a]	–	–	[49]
$MAPbCl_3$	Cubic	(1 0 0)	19.8(7)	0.29(2)	19.4[a,b]	–	–	[49]
		(1 1 0)	17.4(7)	0.25(2)	17.1[a,b]	–		[49]

[a] Estimated for a homogeneous, isotropic, and linear elastic material, according to: $B = E/3(1-2\nu)$ [42].
[b] Estimated values $\nu = 0.33$.

indicates significant elastic anisotropy in $Cs_2AgBiBr_6$. Comparatively, the E values of $Cs_2AgBiBr_6$ are larger than those from the cubic Pm-3m $MAPbBr_3$ (Table S2) along the respective crystallographic directions with the Young's moduli normal to (1 0 0), (1 1 0) and (1 1 1) planes being ~24.3%, 5.5% and 2.9% larger, respectively. As reported in a previous work [25], the Ag-Br and Bi-Br bond lengths in $Cs_2AgBiBr_6$ are 2.821 and 2.814 Å respectively, while the Pb-Br bond length in $MAPbBr_3$ is 2.950 Å, i.e., the metal-bromide bonds in the former are 4.37% and 4.61% shorter than that in the latter. As a result, the corresponding bond strengths in the $[AgBiBr_6]^{2-}$ framework can be expected to be stronger than those in the $[PbBr_3]^-$framework. This is probably the reason for the observed higher framework stiffness in $Cs_2AgBiBr_6$. A comparision of the mechanical properties of $Cs_2AgBiBr_6$ with its single perovskite counterpart, $CsPbBr_3$, suggests that the former is much stiffer although they are in different space groups ($CsPbBr_3$ is orthorhombic at room temperature) [42].

To further probe the elastic anisotropy, we simplified the perovskite structure to a simple cubic framework motif by noting that the bcc structure can be obtained by the superposition of two simple cubic structures and treating the Ag-X-Bi linkages as springs. When the springs are connected in parallel, the total stiffness coefficient, $k_{total,}$ equals the sum of the individual spring constants, i.e., $k_{total} = \Sigma k_i$. On the other hand, when the springs are arranged in series, $1/k_{total} = \Sigma 1/k_i$ (see SI for details). On this basis, the uniaxial deformation response of the perovskite structure when stressed along the axial, face-diagonal, and body-diagonal directions, as displayed in Fig. 2, can be disassociated as described in Fig. S3. This simple analysis shows that for parallel and tandem arrangement of springs, k_{total} = 4, 2, 1.2 times k along ⟨1 0 0⟩, ⟨1 1 0⟩,and ⟨1 1 1⟩ directions, respectively (see SI for details), where k is the stiffness coefficient of each spring. Since E is proportional to k, this expected anisotropy in E is consistent with those made using DFT calculations, i.e., $E(1\,0\,0) > E(1\,1\,0) > E(1\,1\,1)$. The differences between the spring model and first principles calculations arise from the deviation between the classical and quantum mechanics.

In order to verify the aforementioned theoretical results, we performed nanoindentation experiments, so as to extract the

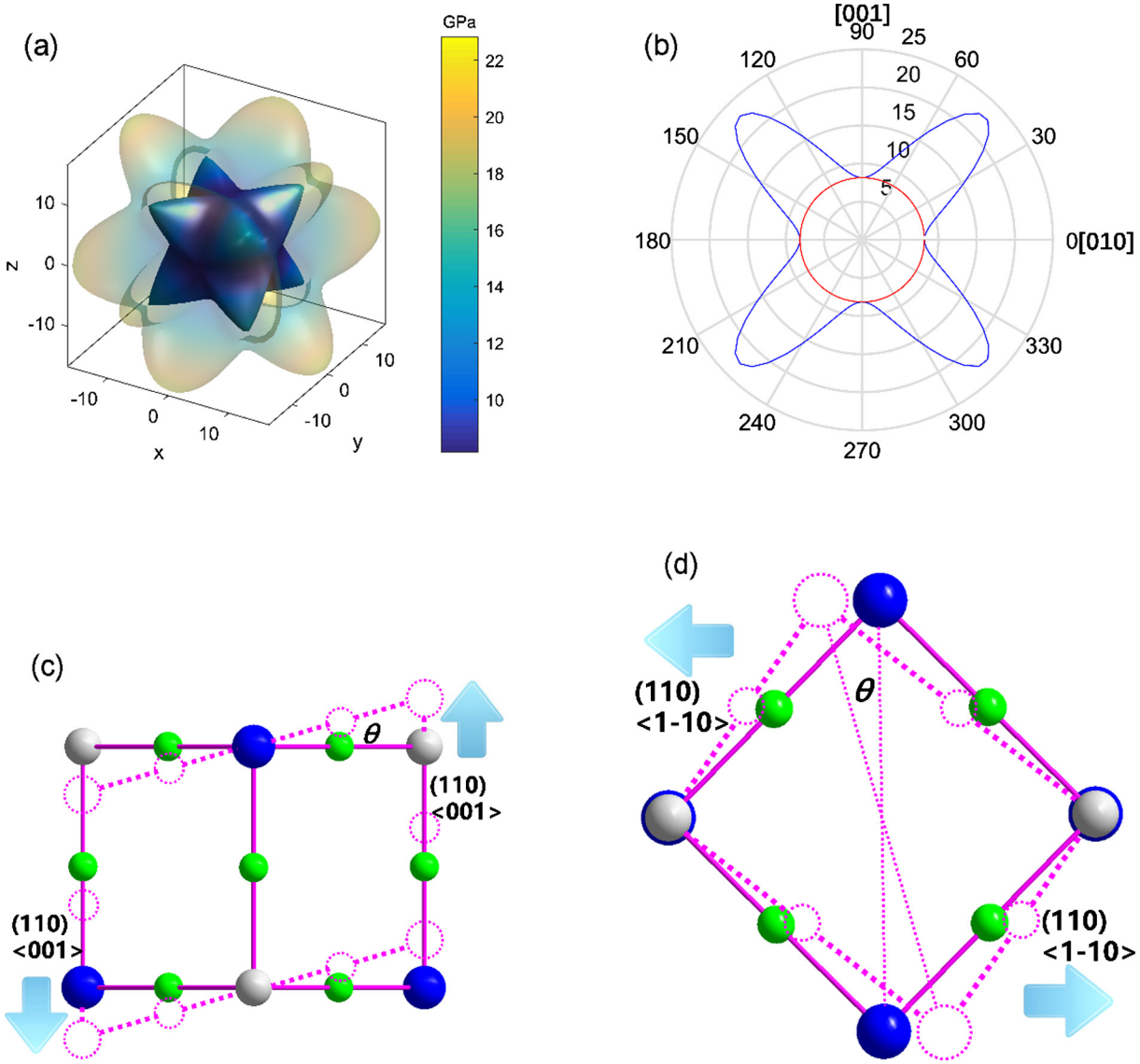

Fig. 4. Shear modulus (G) representation surfaces extracted from DFT calculations. (a) 3D surface of G_{max} and G_{min}. The transparent outer and non-transparent inner layers mean the maximum and minimum values, respectively. (b) 2D polar plots of G_{max} and G_{min} projected normal to the (1 0 0) plane. 0 and 90° are along the [0 1 0] and [0 0 1], respectively. The blue outer and red inner lines mean the maximum and minimum values. (c), (d) Schematic diagrams of the (1 1 0) plane sheared along ⟨0 0 1⟩ and ⟨1 −1 0⟩ directions. Color codes: Bi, blue; Ag, gray; Br, green; solid lines: original edge; dashed lines: sheared edge. θ is the deformation angle between the original and sheared planes. (For interpretation of the references to color in this figure legend, the reader is referred to the web version of this article.)

Young's modulus of $Cs_2AgBiBr_6$ single-crystals. Representative load-indentation depth (*P-h*) curve obtained on the (1 1 1) face is shown in Fig. 3. The maximum surface penetration depth was about 538 nm, which occurs at the maximum load of 5 mN that was held for 10 s. As listed in Table S3, the average experimentally obtained *E* on the (1 1 1) face is 22.6(6) GPa, which is close to that 22.3 GPa calculated using DFT, indicating the validity of our first principles approach.

The experimental values of *E*, hardnesses (*H*), *B*, phase transition pressure (P_c) and linear thermal expansion coefficients (α) are listed for all known solar cell perovskites in Table 2. It is clear that *E* of $Cs_2AgBiBr_6$ is significantly higher than those of hybrid halide double perovskites MA_2MBiX_6 (M = K, Ag, Tl; X = Cl, Br), which indicates that the denser Cs-based double perovskite is the stiffest [12]. Additionally, a comparison with those of hybrid lead halide perovskites $MAPbX_3$ (X = Cl, Br or I) shows that the *E* and *H* values of $Cs_2AgBiBr_6$ are also much higher due to the fact that the bond lengths of Ag-Br and Bi-Br in the latter are shorter than those of Pb-X (X = Cl [44], Br [45] or I [46]) in the former.

The shear modulus (*G*) of a material indicates its resistance to shape change through distortion under shear loading. Variations of *G*, extracted from the DFT calculations, in 3D and a 2D polar plot that was projected normal to the (1 0 0) plane, are displayed in Fig. 4(a) and (b) respectively. From them, it is seen that G_{min} occurs when (1 1 0) plane is sheared along ⟨0 0 1⟩, while G_{max} arises from the shearing of the same plane, but along ⟨1 −1 0⟩. These two extrema in *G*, i.e., G_{min} (8.15 GPa) and G_{max} (22.82 GPa), are equal to C_{44} and $(C_{11} - C_{12})/2$, respectively, which is expected for a cubic crystal [36]. The anisotropy in *G* of $Cs_2AgBiBr_6$, given by the ratio of G_{max} to G_{min}, is 2.80. Such an high ratio again confirms that this material is significantly anisotropic. As compared to E_{min} (22.33 GPa), G_{min} is ~64% smaller, which implies that $Cs_2AgBiBr_6$ is most vulnerable to shearing. This observation is particularly important in the context of manufacturing, as it demands special attention for aspects such as shear-induced plasticity, amorphization and rapture. However, *G* of $Cs_2AgBiBr_6$ are slightly larger than those of $MAPbBr_3$ in any direction [25], and the shear moduli *G* (1 0 0)<*h k l*>(G_{min}), *G*(1 1 1)<*h k l*>, and G_{max} of $Cs_2AgBiBr_6$ are 0.6%, 10.5% and 24.0% larger than those from the same orientations of $MAPbBr_3$. Similar to the origin of anisotropy in *E*, the shorter Ag-Br and Bi-Br bond lengths, compared with Pb-Br in $MAPbBr_3$, are responsible for the higher *G* values in $Cs_2AgBiBr_6$. Since the *G* values along *G*(1 1 1)<*h k l*> directions are more sensitive to the change of bond lengths in the perovskite framework, these orientations exhibit the largest enhancement in *G* as compared with those from $MAPbBr_3$.

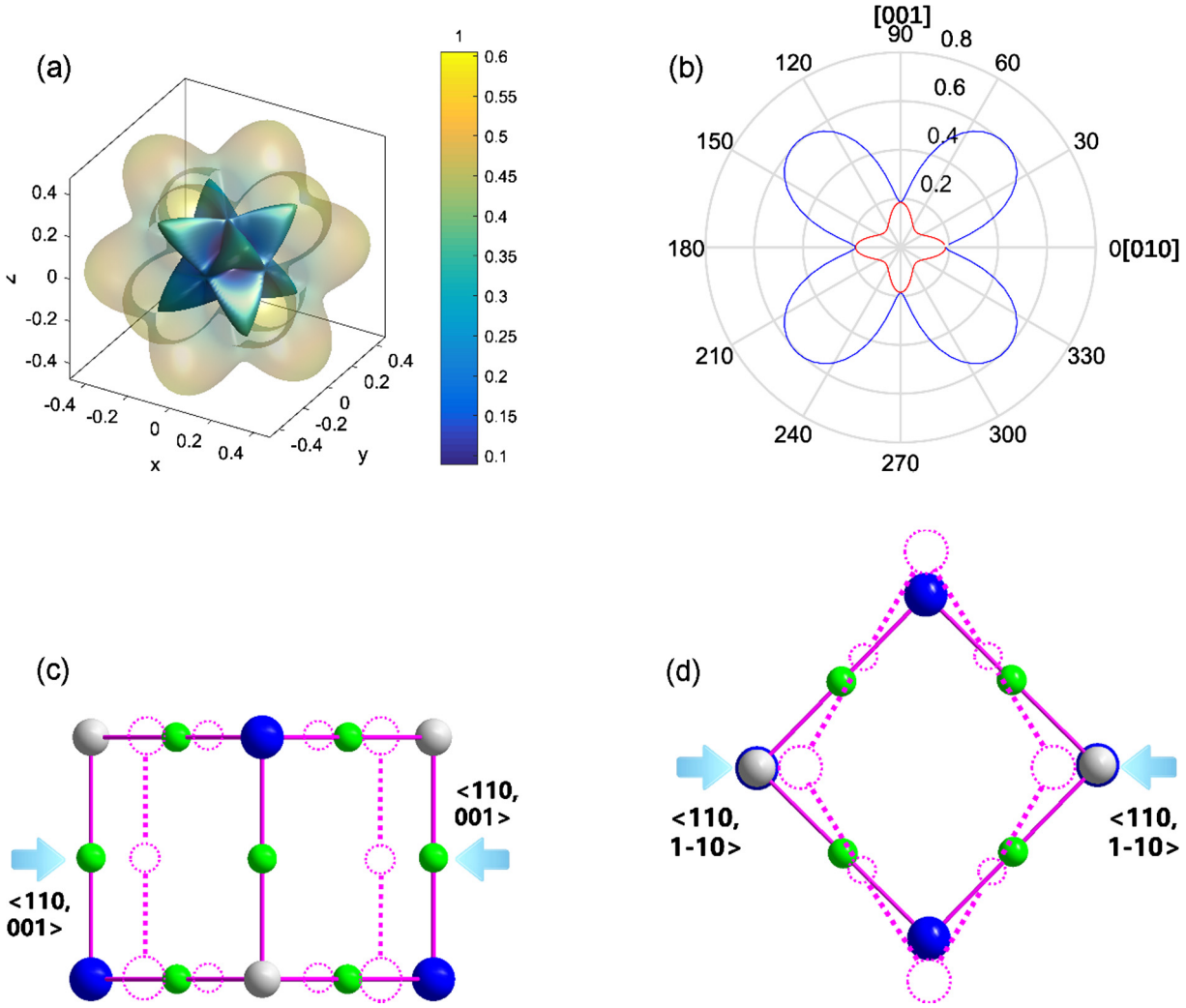

Fig. 5. Poisson's ratio (ν) representation surfaces derived from DFT calculations. (a) 3D surface of ν_{max} and ν_{min}. The transparent outer and non-transparent inner layers mean the maximum and minimum values, respectively. (b) 2D polar plots of ν_{max} and ν_{min} projected normal to the (1 0 0) plane. 0 and 90° are along the [0 1 0] and [0 0 1], respectively. The blue outer and red inner lines mean the maximum and minimum values. (c), (d) Schematic diagram of Poisson's ratios show the transverse strain of ⟨0 0 1⟩ and ⟨1 −1 0⟩ directions respectively, when the stresses all work along the ⟨1 1 0⟩. Color codes: Bi, blue; Ag, gray; Br, green; solid lines: original edge; dashed lines: deformation edge. (For interpretation of the references to color in this figure legend, the reader is referred to the web version of this article.)

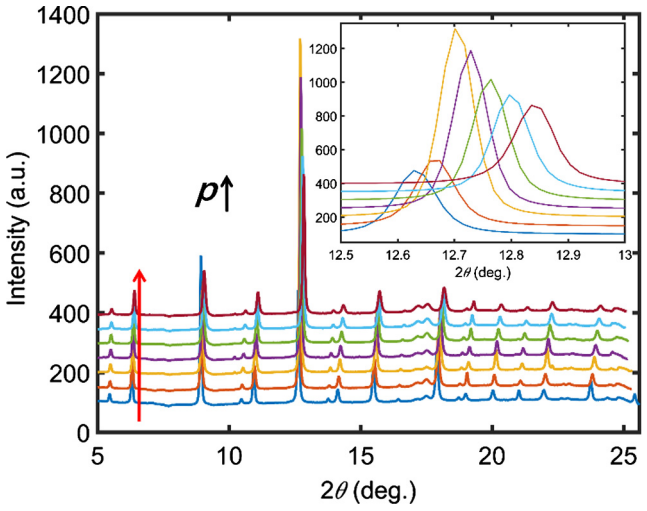

Fig. 6. The representative synchrotron powder diffraction patterns of $Cs_2AgBiBr_6$ at 0, 0.33, 0.49, 0.66, 0.91, 1.15 and 1.57 GPa, respectively, at room temperature. The inset shows the right shift of the strongest Bragg peak (0 0 1) as a function of pressure.

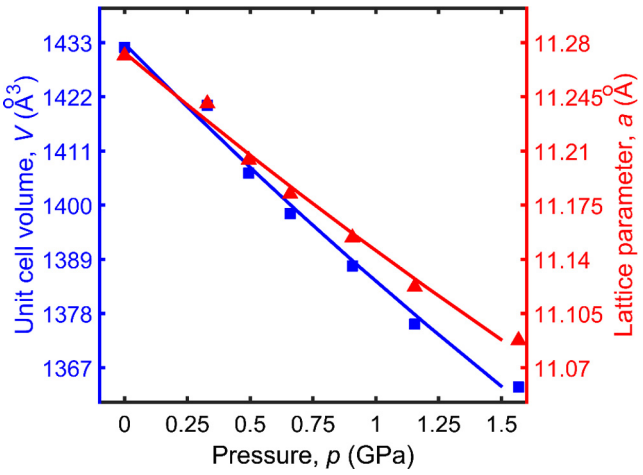

Fig. 7. The evolution of unit cell volume (V) (blue and filled squares) and the cubic axis (a) length (red and filled triangles) as a function of pressure. The errors are smaller than the experimental data points. The solid lines represent the 2nd – order Birch – Murnaghan fits to the experimental data. (For interpretation of the references to color in this figure legend, the reader is referred to the web version of this article.)

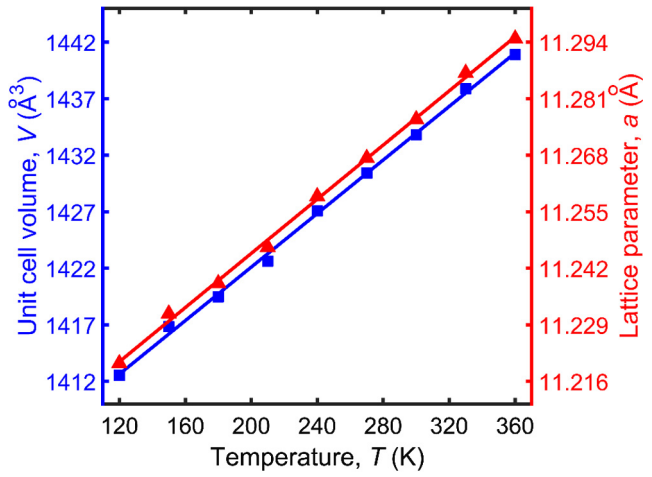

Fig. 8. The evolution of unit cell volume (V) (blue and filled squares) and the cubic axis (a) length (red and filled triangles) as a function of temperature. The errors are smaller than the experimental data points. The solid lines represent the linear fits to the experimental data [43]. (For interpretation of the references to color in this figure legend, the reader is referred to the web version of this article.)

The mechanistic reasons for the observed high anisotropy in G can be understood by examining the underlying framework structure. When any given crystallographic plane in the cubic structure is sheared, the shear strains on (1 0 0) or (1 1 1) remain isotropic because of the high symmetry present in the *Fm*-3*m* space group. This is not the case, however, for shearing on (1 1 0) due to a much lower symmetry in the arrangement of atoms in the perovskite unit cell. As seen in Fig. 4(c) and (d), the shear strain (γ), which is defined as the angle of deformation (θ), is directly related to the bond length changes of the perovskite structure. Specifically, the variation of bond lengths (Δx) is proportional to the square of deformation angle (θ) when the (1 1 0) plane is sheared along ⟨0 0 1⟩ (Fig. 4c), but proportional to θ for (1 1 0)⟨1 −1 0⟩ shear (Fig. 4d), as derived by the Taylor series expansion. As θ is small, a much larger shear stress is needed for deformation along ⟨1 −1 0⟩ as compared to that along ⟨0 0 1⟩ for obtaining same θ. This leads to the observed G_{min} along ⟨0 0 1⟩ and G_{max} along ⟨1 −1 0⟩. Furthermore, shearing of (1 0 0) and (1 1 1) planes along any direction is similar to that depicted in Fig. 4(c) and (d), and the extracted results, from DFT, show that $G(1\,0\,0)\langle h\,k\,l\rangle = G_{min}$ and $G(1\,1\,1)\langle h\,k\,l\rangle$ = 14.26 GPa, which is intermediate to those of G_{max} and G_{min}.

We turn our attention next to the Poisson's ratios (ν), which are defined as the ratio of the transverse strains (ε_j) to the axial strains (ε_i), $\nu = -\varepsilon_j/\varepsilon_i$ [54,55]. The values and representation surfaces of ν in $Cs_2AgBiBr_6$ are given in Table 1 and Fig. 5(a) and (b), respectively. From them, it is seen that ν ranges from 0.09 to 0.61. Notably, the maximum in ν decreases from Cl to I while the minimum remains invariant. This observation implies that the Ag-X and Bi-X (X = Cl, Br or I) bonds exert relatively lesser influence on the anisotropy in ν as compared with E and G.

Interestingly, ν of $Cs_2AgBiBr_6$ are similar to those of $MAPbBr_3$, which are in the range of 0.10–0.53 [25]. This similarity is probably due to the same cubic symmetry since ν are more influenced by the crystal symmetry rather than the strengths of chemical bonds. For a ductile material, a high value of ν (typically above 0.26 [25]) is preferable. Since a high value of 0.61 for ν is noted in <110, 1 −1 0>, $Cs_2AgBiBr_6$ may not be brittle. Nevertheless, the significant amount of directions along which ν less than the critical value (i.e. ν<110,001> = 0.09) could lead to brittleness, a vital factor which needs to be taken into account for device design.

The anisotropic nature of ν can also be understood by recourse to the underlying crystal structure and the spring model that was alluded to earlier in this paper. When the crystal is subjected to uniaxial compression along ⟨1 1 0⟩, the transverse strains along ⟨0 0 1⟩ and ⟨1 −1 0⟩ are infinitely small and finitely small quantities respectively, as depicted in Fig. 5(c) and (d). As a result, strains in ⟨1 −1 0⟩ are much larger than those in ⟨0 0 1⟩, which cause ν to be maximum along ⟨1 −1 0⟩ and minimum along ⟨0 0 1⟩.

The bulk modulus (B) is a material parameter that indicates the resistance it offers to volume change (whereas the shear modulus indicates the resistance to shape change). Our DFT calculations show that B of Cs_2AgBiX_6 scales inversely with the atomic radius of X (Table 1). This observation is consistent with the trends in both the strengths of Ag-X and Bi-X bonds. To examine the validity of the DFT estimates, we performed HP-PXRD experiments on $Cs_2AgBiBr_6$ crystals in a synchrotron facility, the results of which are displayed in Fig. 6. As seen from it, all the diffraction peaks shift to higher angles as the pressure (P) is increased from atmospheric to 1.57 GPa, with no indication of any phase transition. For

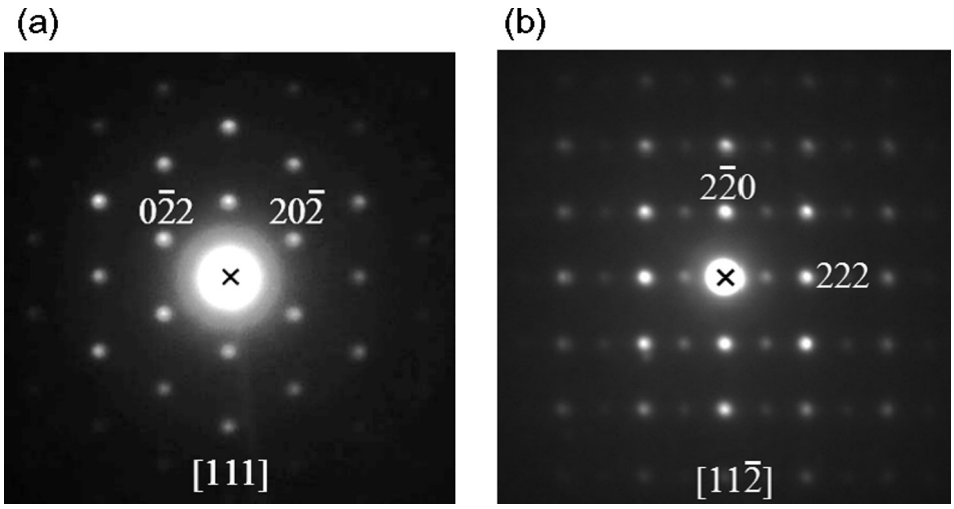

Fig. 9. SAED patterns of $Cs_2AgBiBr_6$ single crystal along [1 1 1] (a) and [1 1 −2] (b) zone axes.

contrast, a pressure-induced phase transition was reported to occur at about 0.3 GPa in $MAPbI_3$ and at 0.4 GPa in $MAPbBr_3$ [53,56]. Thus, $Cs_2AgBiBr_6$ shows considerably more resistance to any such phase transition under hydrostatic compression.

Variations in the unit cell volume (V) and lattice parameter (a) of $Cs_2AgBiBr_6$ with P are displayed in Fig. 7. From it, we note that both V and a get reduced by ~4.8% and ~1.6% respectively, when P is increased from atmospheric to 1.57 GPa. By fitting the V-P data with the second order Birch - Murnaghan equation of state [57–59], a value of 27.3(1.4) GPa is obtained for B, which is in excellent agreement with the DFT estimated value of 28.6 GPa, which not only validates the DFT calculations but also confirms the inference that we draw from it, namely resistance to high volumetric changes of the framework lattice stems from the Ag-X and Bi-X bond strengths.

3.2. Thermal expansion behavior

The thermal expansion behavior of $Cs_2AgBiBr_6$ is examined next, as it also depends intimately on the crystal structures and the bond strengths, just like the elastic properties. For this purpose, VT-SCXRD data of $Cs_2AgBiBr_6$ were collected from 120 to 360 K at 30 K intervals. Variations in the obtained cell parameters with temperature (T) are displayed in Fig. 8, from which it is seen that both cell volume (V) and axis length (a) vary linearly and positively with T. Upon increasing T from 120 to 360 K, a increases by about 0.67% and V increases by 2.01%. Linear fits through the experimental data yield the coefficients of linear (α_a) and volumetric (α_V) thermal expansion for $Cs_2AgBiBr_6$ as 27.8(3) and 83.9(10) MK^{-1}, respectively [59]. These properties are compared with respective values of other perovskites in Table 2, from which it is seen that α_a of $Cs_2AgBiBr_6$ is about 26.3%, 36.8%, 35.8% and 17.0% lower than those from the $CsPbBr_3$, $(MA)_2AgBiBr_6$, $MAPbI_3$ and $MAPbBr_3$, respectively. Such significantly lower thermal expansion of $Cs_2AgBiBr_6$ arises from the stronger bonding characteristics and the absence of organic components, which impart higher structural stiffness and less susceptible to temperature perturbation. These observations are consistent with the strong and sharp electron diffraction spots in the TEM patterns (Fig. 9) which are in marked difference with the existence of diffuse scattering in HOIPs arising from light organic compositions, such as $MAPbI_3$ [60]. Importantly, a lower thermal expansion behavior can minimize the thermal strains that could potentially arise either during processing or in service, in turn enhancing the device life [42,61].

4. Summary and conclusions

In summary, we have examined the elastic and thermal properties of lead-free halide double perovskite $Cs_2AgBiBr_6$ in detail *via* DFT calculations, which were validated with complementary experimental characterizations. The Young's moduli, shear moduli and Poisson's ratios of $Cs_2AgBiBr_6$ along all crystallographic directions were mapped by using the obtained full elastic constants and the observed elastic anisotropy was rationalized by recourse to structural analysis from an atomic level. The obtained results demonstrate that the mechanical and thermal performance of $Cs_2AgBiBr_6$ is significantly better as compared to other $MAPbBr_3$ type perovskites. VT-SCXRD experiments confirm that $Cs_2AgBiBr_6$ exhibiting about 20% smaller uniaxial and volumetric thermal expansion as compared with $MAPbBr_3$. The higher framework stiffness of the former is due to the presence of relatively stronger Ag-Br and Bi-Br bonds in the former whereas the Pb-X (X = Cl, Br or I) bonds in the metal halide perovskites are relatively weaker. The superior stiffness and thermal expansion behavior of $Cs_2AgBiBr_6$ combined with its nontoxicity and impressive moisture stability makes it a strong candidate for potential applications in optoelectronics and photovoltaics.

Acknowledgements

The authors acknowledge funding support from the National Natural Science Foundation of China (Grant Nos. 21571072, 11374114, 10974062). F. Wei is a holder for A∗STAR international fellowship granted by Agency for Science, Technology and Research, Singapore. S. Sun and Z. Deng would like to thank the Cambridge Overseas trust and China Scholarship Council.

Appendix A. Supplementary material

Supplementary data associated with this article can be found, in the online version, at http://dx.doi.org/10.1016/j.commatsci.2017.09.014.

References

[1] W. Li, Z. Wang, F. Deschler, S. Gao, R.H. Friend, A.K. Cheetham, Chemically diverse and multifunctional hybrid organic–inorganic perovskites, Nat. Rev. Mater. 2 (2017) 16099.
[2] T.M. Brenner, D.A. Egger, L. Kronik, G. Hodes, D. Cahen, Hybrid organic—inorganic perovskites: low-cost semiconductors with intriguing charge-transport properties, Nat. Rev. Mater. 1 (2016) 16011.

[3] S.D. Stranks, H.J. Snaith, Metal-halide perovskites for photovoltaic and light-emitting devices, Nat. Nanotechnol. 10 (5) (2015) 391–402.
[4] B. Saparov, D.B. Mitzi, Organic-inorganic perovskites: structural versatility for functional materials design, Chem. Rev. 116 (7) (2016) 4558–4596.
[5] A. Kojima, K. Teshima, Y. Shirai, T. Miyasaka, Organometal halide perovskites as visible-light sensitizers for photovoltaic cells, J. Am. Chem. Soc. 131 (2009) 6050–6051.
[6] F. Hao, C.C. Stoumpos, D.H. Cao, R.P.H. Chang, M.G. Kanatzidis, Lead-free solid-state organic–inorganic halide perovskite solar cells, Nat. Photon. 8 (6) (2014) 489–494.
[7] N.K. Noel, S.D. Stranks, A. Abate, C. Wehrenfennig, S. Guarnera, A.A. Haghighirad, A. Sadhanala, G.E. Eperon, S.K. Pathak, M.B. Johnston, A. Petrozza, L.M. Herz, H.J. Snaith, Lead-free organic–inorganic tin halide perovskites for photovoltaic applications, Energy Environ. Sci. 7 (9) (2014) 3061.
[8] W.S. Yang, J.H. Noh, N.J. Jeon, Y.C. Kim, S. Ryu, J. Seo, S.I. Seok, High-performance photovoltaic perovskite layers fabricated through intramolecular exchange, Science 348 (6240) (2015) 1234–1237.
[9] A. Babayigit, A. Ethirajan, M. Muller, B. Conings, Toxicity of organometal halide perovskite solar cells, Nat. Mater. 15 (3) (2016) 247–251.
[10] F. Wei, Z. Deng, S. Sun, F. Xie, G. Kieslich, D.M. Evans, M.A. Carpenter, P.D. Bristowe, A.K. Cheetham, The synthesis, structure and electronic properties of a lead-free hybrid inorganic–organic double perovskite $(MA)_2KBiCl_6$(MA = methylammonium), Mater. Horiz. 3 (4) (2016) 328–332.
[11] Z. Deng, F. Wei, S. Sun, G. Kieslich, A.K. Cheetham, P.D. Bristowe, Exploring the properties of lead-free hybrid double perovskites using a combined computational-experimental approach, J. Mater. Chem. A 4 (31) (2016) 12025–12029.
[12] F. Wei, Z. Deng, S. Sun, F. Zhang, D.M. Evans, G. Kieslich, S. Tominaka, M.A. Carpenter, J. Zhang, P.D. Bristowe, A.K. Cheetham, Synthesis and properties of a lead-free hybrid double perovskite: $(CH_3NH_3)_2AgBiBr_6$, Chem. Mater. 29 (3) (2017) 1089–1094.
[13] A.H. Slavney, T. Hu, A.M. Lindenberg, H.I. Karunadasa, A bismuth-halide double perovskite with long carrier recombination lifetime for photovoltaic applications, J. Am. Chem. Soc. 138 (7) (2016) 2138–2141.
[14] E.T. McClure, M.R. Ball, W. Windl, P.M. Woodward, Cs_2AgBiX_6 (X = Br, Cl): new visible light absorbing, lead-free halide perovskite semiconductors, Chem. Mater. 28 (5) (2016) 1348–1354.
[15] G. Volonakis, M.R. Filip, A.A. Haghighirad, N. Sakai, B. Wenger, H.J. Snaith, F. Giustino, Lead-free halide double perovskites via heterovalent substitution of noble metals, J. Phys. Chem. Lett. 7 (7) (2016) 1254–1259.
[16] Z. Xiao, W. Meng, J. Wang, Y. Yan, Thermodynamic stability and defect chemistry of bismuth-based lead-free double perovskites, ChemSusChem 9 (18) (2016) 2628–2633.
[17] F. Giustino, H.J. Snaith, Toward lead-free perovskite solar cells, ACS Energy Lett. 1 (2016) 1233–1240.
[18] G. Volonakis, A.A. Haghighirad, R.L. Milot, W.H. Sio, M.R. Filip, B. Wenger, M.B. Johnston, L.M. Herz, H.J. Snaith, F. Giustino, $Cs_2InAgCl_6$: a new lead-free halide double perovskite with direct band gap, J. Phys. Chem. Lett. 8 (2017) 772–778.
[19] A.M. Rappe, K.M. Rabe, E. Kaxiras, J.D. Joannopoulos, Optimized pseudopotentials, Phys. Rev. B 41 (2) (1990) 1227–1230.
[20] J.P. Perdew, K. Burke, M. Ernzerhof, Generalized gradient approximation made simple, Phys. Rev. Lett. 77 (18) (1996) 3865.
[21] U.V. Barth, L. Herbin, A local exchange-correlation potential for the spin polarized case. I, J. Phys. C: Solid State Phys. 5 (1972) 1629.
[22] B. Hammer, L.B. Hansen, J.K. Norskov, Improved adsorption energetics within density-functional theory using revised Perdew-Burke-Ernzerhof functionals, Phys. Rev. B 59 (1999) 7413–7421.
[23] J.P. Perdew, J.A. Chevary, S.H. Vosko, K.A. Jackson, M.R. Pederson, D.J. Singh, C. Fiolhais, Atoms, molecules, solids, and surfaces: applications of the generalized gradient approximation for exchange and correlation, Phys. Rev. B 46 (11) (1992) 6671–6687.
[24] D.A. Egger, L. Kronik, Role of dispersive interactions in determining structural properties of organic-inorganic halide perovskites: insights from first-principles calculations, J. Phys. Chem. Lett. 5 (15) (2014) 2728–2733.
[25] J. Feng, Mechanical properties of hybrid organic-inorganic $CH_3NH_3BX_3$ (B = Sn, Pb; X = Br, I) perovskites for solar cell absorbers, APL Mater. 2 (8) (2014) 081801.
[26] H.J. Monkhorst, Special points for Brillouin-zone integrations, Phys. Rev. B 13 (12) (1976) 5188–5192.
[27] B.G. Pfrommer, M. Côté, S.G. Louie, M.L. Cohen, Relaxation of crystals with the quasi-Newton method, J. Comput. Phys. 131 (1) (1997) 233–240.
[28] Y. Le Page, P. Saxe, Symmetry-general least-squares extraction of elastic data for strained materials from ab initio calculations of stress, Phys. Rev. B 65 (10) (2002).
[29] M.R. Filip, S. Hillman, A.A. Haghighirad, H.J. Snaith, F. Giustino, Band gaps of the lead-free halide double perovskites $Cs_2BiAgCl_6$ and $Cs_2BiAgBr_6$ from theory and experiment, J. Phys. Chem. Lett. 7 (13) (2016) 2579–2585.
[30] U. Ramamurty, J.-I. Jang, Nanoindentation for probing the mechanical behavior of molecular crystals – a review of the technique and how to use it, CrystEngComm 16 (1) (2014) 12–23.
[31] S. Varughese, M.S. Kiran, U. Ramamurty, G.R. Desiraju, Nanoindentation in crystal engineering: quantifying mechanical properties of molecular crystals, Angew. Chem. Int. Ed. Engl. 52 (10) (2013) 2701–2712.
[32] W.C. Oliver, G.M. Pharr, An improved technique for determining hardness and elastic modulus using load and displacement sensing indentation experiments, J. Mater. Res. 7 (6) (1992) 1564–1583.
[33] Z.-J. Wu, E.-J. Zhao, H.-P. Xiang, X.-F. Hao, X.-J. Liu, J. Meng, Crystal structures and elastic properties of superhard IrN_2 and IrN_3 from first principles, Phys. Rev. B 76 (5) (2007).
[34] J.C. Tan, B. Civalleri, C.C. Lin, L. Valenzano, R. Galvelis, P.F. Chen, T.D. Bennett, C. Mellot-Draznieks, C.M. Zicovich-Wilson, A.K. Cheetham, Exceptionally low shear modulus in a prototypical imidazole-based metal-organic framework, Phys. Rev. Lett. 108 (9) (2012) 095502.
[35] F. Mouhat, F.-X. Coudert, Necessary and sufficient elastic stability conditions in various crystal systems, Phys. Rev. B 90 (22) (2014) 224104.
[36] G. Feng, X. Jiang, W. Wei, P. Gong, L. Kang, Z. Li, Y. Li, X. Li, X. Wu, Z. Lin, W. Li, P. Lu, High pressure behaviour and elastic properties of a dense inorganic-organic framework, Dalton Trans. 45 (10) (2016) 4303–4308.
[37] A. Marmier, Z.A.D. Lethbridge, R.I. Walton, C.W. Smith, S.C. Parker, K.E. Evans, ElAM: a computer program for the analysis and representation of anisotropic elastic properties, Comput. Phys. Commun. 181 (12) (2010) 2102–2115.
[38] C.G. Ma, M.G. Brik, Hybrid density-functional calculations of structural, elastic and electronic properties for a series of cubic perovskites $CsMF_3$ (M=Ca, Cd, Hg, and Pb), Comp. Mater. Sci. 58 (2012) 101–112.
[39] R.S. Mulliken, Electronic population analysis on LCAO-MO molecular wave functions. I, J. Chem. Phys. 23 (10) (1955) 1833.
[40] F.L. Hirshfeld, Bonded-atom fragments for describing molecular charge densities, Theor. Chem. Acc. 44 (2) (1977) 129–138.
[41] S. Saha, R.K. Roy, P.W. Ayers, Are the Hirshfeld and Mulliken population analysis schemes consistent with chemical intuition?, Int J. Quantum. Chem. 109 (9) (2009) 1790–1806.
[42] Y. Rakita, S.R. Cohen, N.K. Kedem, G. Hodes, D. Cahen, Mechanical properties of $APbX_3$ (A = Cs or CH_3NH_3; X = I or Br) perovskite single crystals, MRS Commun. 5 (04) (2015) 623–629.
[43] W. Li, A. Thirumurugan, P.T. Barton, Z. Lin, S. Henke, H.H. Yeung, M.T. Wharmby, E.G. Bithell, C.J. Howard, A.K. Cheetham, Mechanical tunability via hydrogen bonding in metal-organic frameworks with the perovskite architecture, J. Am. Chem. Soc. 136 (22) (2014) 7801–7804.
[44] Y. Kawamura, H. Mashiyama, Modulated structure in phase II of $CH_3NH_3PbCl_3$, J. Korean Phys. Soc. 35 (6) (1999).
[45] P. Zhao, J. Xu, X. Dong, L. Wang, W. Ren, L. Bian, A. Chang, Large-size $CH_3NH_3PbBr_3$ single crystal: growth and In situ characterization of the photophysics properties, J. Phys. Chem. Lett. 6 (13) (2015) 2622–2628.
[46] C.C. Stoumpos, C.D. Malliakas, M.G. Kanatzidis, Semiconducting tin and lead iodide perovskites with organic cations: phase transitions, high mobilities, and near-infrared photoluminescent properties, Inorg. Chem. 52 (15) (2013) 9019–9038.
[47] M. Rodová, J. Brožek, K. Knížek, K. Nitsch, Phase transitions in ternary caesium lead bromide, J. Therm Anal Calorim 71 (2) (2003) 667–673.
[48] Y. Kawamura, H. Mashiyama, K. Hasebe, Structural study on cubic–tetragonal transition of $CH_3NH_3PbI_3$, J. Phys. Soc. JPN 71 (7) (2002) 1694–1697.
[49] S. Sun, Y. Fang, G. Kieslich, T.J. White, A.K. Cheetham, Mechanical properties of organic–inorganic halide perovskites, $CH_3NH_3PbX_3$(X = I, Br and Cl), by nanoindentation, J. Mater. Chem. A 3 (36) (2015) 18450–18455.
[50] M. Szafranski, A. Katrusiak, Mechanism of pressure-induced phase transitions, amorphization, and absorption-edge shift in photovoltaic methylammonium lead iodide, J. Phys. Chem. Lett. 7 (17) (2016) 3458–3466.
[51] A. Jaffe, Y. Lin, C.M. Beavers, J. Voss, W.L. Mao, H.I. Karunadasa, High-pressure single-crystal structures of 3D lead-halide hybrid perovskites and pressure effects on their electronic and optical properties, ACS Cent. Sci. 2 (4) (2016) 201–209.
[52] H. Mashiyama, Y. Kawamura, E. Magome, Y. Kubota, Displacive character of the cubic-tetragonal transition in $CH_3NH_3PbX_3$, J. Korean Phys. Soc. 42 (2003) S1026–S1029.
[53] Y. Wang, X. Lu, W. Yang, T. Wen, L. Yang, X. Ren, L. Wang, Z. Lin, Y. Zhao, Pressure-induced phase transformation, reversible amorphization, and anomalous visible light response in organolead bromide perovskite, J. Am. Chem. Soc. 137 (34) (2015) 11144–11149.
[54] M.R. Ryder, J.C. Tan, Explaining the mechanical mechanisms of zeolitic metal-organic frameworks: revealing auxeticity and anomalous elasticity, Dalton Trans. 45 (10) (2016) 4154–4161.
[55] M. Wang, X. Zhang, Y. Chen, D. Li, How guest molecules stabilize the narrow pore phase of soft porous crystals: structural and mechanical properties of MIL-53(Al)⊃H_2O, J. Phys. Chem. C 120 (9) (2016) 5059–5066.
[56] I.P. Swainson, M.G. Tucker, D.J. Wilson, B. Winkler, S. Milman, Pressure response of an organic-inorganic perovskite methylammonium lead bromide, Chem. Mater. 19 (2007) 2401–2405.
[57] F.D. Murnaghan, The compressibility of media under extreme pressures, Proc. Natl. Acad. Sci. USA 30 (9) (1944) 244–247.
[58] F. Birch, Finite elastic strain of cubic crystals, Phys. Rev. 71 (11) (1947) 809–824.
[59] M.J. Cliffe, A.L. Goodwin, PASCal: a principal-axis strain calculator for thermal expansion and compressibility determination, J. Appl. Cryst. 45 (2012) 1321–1329.
[60] A. Fakharuddin, F. Di Giacomo, I. Ahmed, Q. Wali, T.M. Brown, R. Jose, Role of morphology and crystallinity of nanorod and planar electron transport layers on the performance and long term durability of perovskite solar cells, J. Power Sources 283 (2015) 61–67.
[61] M.U. Rothmann, W. Li, Y. Zhu, U. Bach, L. Spiccia, J. Etheridge, Y.B. Cheng, Direct observation of intrinsic twin domains in tetragonal $CH_3NH_3PbI_3$, Nat. Commun. 8 (2017) 14547.